Measuring the Charge State of an Adatom with Noncontact Atomic Force Microscopy

Leo Gross, *et al.*

Science **324**, 1428 (2009);
DOI: 10.1126/science.1172273

the concentration of carriers distributed throughout the generating range of the electron beam [$\Delta n(z)$].

$$I_{CL} \propto \int_V \frac{\Delta n(z)}{\tau_r} dz \quad (1)$$

In this formula, τ_r is the life of the carriers that contribute to radiative recombination, V is the generation volume, and z is a depth. On the basis of this assumption, the CL intensity (I_{CL}) is simply proportional to the film thickness. The expected CL intensity ratios of ^{13}C to ^{12}C, calculated from the thicknesses of the multilayer structures, are shown in Fig. 4B. All of the experimental data show dramatic decreases, accompanied by a decrease of emission from ^{13}C layers and the related increase from ^{12}C layers. Even for the structures in Fig. 2, C and D, which consist of a ^{12}C single layer in ^{13}C, the intensity (I) ratio $I[^{13}C]/I[^{12}C]$ decreases from 1/2 to 1/3, with respect to the expected ratio. These phenomena indicate that a large diffusion length of the excited carriers plays an important role. Several studies have reported diffusion lengths in natural isotopic mixtures of diamond that range from 500 nm to 250 μm (*29*–*31*). Our results indicate that almost all carriers generated in our samples diffuse at least 175 nm and may diffuse up to several hundred nanometers.

References and Notes

1. H. Ehrenreich, D. Turnbull, Eds., *Solid State Physics: Advances in Research Applications,* vol. 44 (Academic Press, New York, 1991).
2. J. W. Ager III, E. E. Haller, *Phys. Stat. Sol. A* **203**, 3550 (2006).
3. E. E. Haller, *Solid State Commun.* **133**, 693 (2005).
4. K. M. Itoh, E. E. Haller, *Phys. E* **10**, 463 (2001).
5. H. Watanabe, C. E. Nebel, S. Shikata, *Proc. New Diamond Nano Carbons* **2**, 202 (2008).
6. L. Childress *et al.*, *Science* **314**, 281 (2006); published online 13 September 2006 (10.1126/science.1131871).
7. S. Prawer, A. D. Greentree, *Science* **320**, 1601 (2008).
8. Z. Yuan *et al.*, *Science* **295**, 102 (2002); published online 13 December 2001 (10.1126/science.1066790).
9. J. J. L. Morton, *Nat. Phys.* **2**, 365 (2006).
10. T. Gaebel *et al.*, *Nat. Phys.* **2**, 408 (2006).
11. J. R. Maze *et al.*, *Nature* **455**, 644 (2008).
12. J. M. Taylor *et al.*, *Nat. Phys.* **4**, 810 (2008).
13. P. Neumann *et al.*, *Science* **320**, 1326 (2008).
14. V. G. Plekhanov, *Prog. Mater. Sci.* **51**, 287 (2006).
15. F. Widulle *et al.*, *Solid State Commun.* **118**, 1 (2001).
16. M. Cardona, M. L. W. Thewalt, *Rev. Mod. Phys.* **77**, 1173 (2005).
17. H. Watanabe, C. E. Nebel, *Diamond Relat. Mater.* **17**, 511 (2008).
18. A. T. Collins, S. C. Lawson, G. Davies, H. Kanda, *Phys. Rev. Lett.* **65**, 891 (1990).
19. T. Ruf *et al.*, *Solid State Commun.* **105**, 311 (1998).
20. R. Sauer, N. Teofilov, K. Thonke, *Diamond Relat. Mater.* **13**, 691 (2004).
21. T. Kojima, R. Nebashi, K. M. Itoh, Y. Shiraki, *Appl. Phys. Lett.* **83**, 2318 (2003).
22. T. Y. Tan *et al.*, *J. Appl. Phys.* **72**, 5206 (1992).
23. J. Spitzer *et al.*, *Phys. Rev. Lett.* **72**, 1565 (1994).
24. K. Morita *et al.*, *Thin Solid Films* **369**, 405 (2000).
25. M. Nakajima *et al.*, *Phys. Rev. B* **63**, 161304 (2001).
26. Materials and methods are available as supporting material on *Science* Online.
27. K. Kanaya, S. Okayama, *J. Phys. D* **5**, 43 (1972).
28. H. Watanabe *et al.*, *Appl. Phys. Lett.* **73**, 981 (1998).
29. T. Malinauskas *et al.*, *Diamond Relat. Mater.* **17**, 1212 (2008).
30. T. Teraji, S. Yoshizaki, S. Mitani, T. Watanabe, T. Ito, *J. Appl. Phys.* **96**, 7300 (2004).
31. J. Ristein, W. Stein, L. Ley, *Phys. Rev. Lett.* **78**, 1803 (1997).

32. The authors thank N. Fujimori (Diamond Research Center, AIST) and K. Kajimura (Technical Research Institute, Japan Society for the Promotion of Machine Industry) for their support and encouragement during the early days of the study.

Supporting Online Material

www.sciencemag.org/cgi/content/full/324/5933/1425/DC1
Materials and Methods

17 February 2009; accepted 20 April 2009
10.1126/science.1172419

Measuring the Charge State of an Adatom with Noncontact Atomic Force Microscopy

Leo Gross,[1]* Fabian Mohn,[1] Peter Liljeroth,[1,2] Jascha Repp,[1,3] Franz J. Giessibl,[3] Gerhard Meyer[1]

Charge states of atoms can be investigated with scanning tunneling microscopy, but this method requires a conducting substrate. We investigated the charge-switching of individual adsorbed gold and silver atoms (adatoms) on ultrathin NaCl films on Cu(111) using a qPlus tuning fork atomic force microscope (AFM) operated at 5 kelvin with oscillation amplitudes in the subangstrom regime. Charging of a gold atom by one electron charge increases the force on the AFM tip by a few piconewtons. Moreover, the local contact potential difference is shifted depending on the sign of the charge and allows the discrimination of positively charged, neutral, and negatively charged atoms. The combination of single-electron charge sensitivity and atomic lateral resolution should foster investigations of molecular electronics, photonics, catalysis, and solar photoconversion.

Recently, tremendous progress has been made in atomic force microscopy (AFM). For example, chemical sensitivity on the atomic scale (*1*), manipulation of atoms laterally (*2*) and vertically (*3*), and the measurement of lateral forces during atomic manipulation (*4*) have been demonstrated. The resolution of local contact potential difference (LCPD) maps acquired with kelvin probe force microscopy (KPFM) (*5*) has also been pushed to the atomic scale (*6*–*10*).

In this paper, we present the measurement of single-electron charges with atomic resolution by use of AFM. The charge state and charge distribution of adsorbates are an important property that governs many physical and chemical processes and moreover can be exploited in single-electron devices (*11*, *12*). Single-electron devices have attracted considerable attention because they exhibit interesting physical properties and functionalities, such as Coulomb blockade and the Kondo effect. To investigate such devices and the underlying physics at the ultimate spatial limit, it is essential that single-electron charges can be probed directly and with atomic resolution. For example, the ability to map the charge distribution of a single molecular charge-transfer complex will deepen the basic understanding of and advance the search for materials for molecular electronics and organic photovoltaic cells. Furthermore, important insight into catalytic processes will be gained because the charge state also governs the catalytic reactivity of adsorbates (*13*). Most of the systems of relevance in this area involve insulators as a prerequisite to separate charges.

Probing the charge state of single adatoms has recently been demonstrated with scanning tunneling microscopy (STM) (*14*–*16*). However, this indirect measurement requires a conducting tunneling junction, which is incompatible with insulators. In contrast, electrostatic force measurements performed with noncontact AFM (NC-AFM) can achieve single-electron sensitivity (*17*–*23*). In most of these studies, the micromechanical cantilevers have oscillation amplitudes in the 10 to 50 Å regime. Such large amplitudes increase the sensitivity to long-range electrostatic forces but limit the resolution of short-range chemical forces and therefore the spatial resolution. For atomic resolution, oscillation amplitudes on the order of 1 Å are desirable (*24*). In this work, we demonstrate the switching and direct measurement of the charge state of a single atom with AFM. Our approach combines electrostatic force microscopy of single-electron sensitivity with lateral atomic resolution. We image and identify differently charged individual atoms, and measure the difference in

[1]IBM Research, Zurich Research Laboratory, 8803 Rüschlikon, Switzerland. [2]Debye Institute for Nanomaterials Science, Utrecht University, Post Office Box 80000, 3508 TA Utrecht, Netherlands. [3]Institute of Experimental and Applied Physics, University of Regensburg, 93040 Regensburg, Germany.

*To whom correspondence should be addressed. E-mail: lgr@zurich.ibm.com

vertical force and LCPD caused by single-electron charging.

The low-temperature STM/AFM is based on a qPlus sensor design (*25*) operated in ultra-high vacuum at a temperature of ~5 K. A metal tip (*26*) is mounted on the free prong of the tuning fork, and a separate tip wire (that is insulated from the electrodes of the tuning fork) is installed to measure the tunneling current. The bias voltage V is applied to the sample. The high stiffness of the tuning fork [spring constant (k) = 1.8 × 10^3 N/m, resonance frequency (f_0) = 23 kHz, and mechanical quality factor (Q) = 5 × 10^4] allows stable operation at subangstrom oscillation amplitudes A (down to A = 0.2 Å) in the frequency modulation mode (*27*). As a model system, we used single Au and Ag adatoms on 2-monolayer (ML)–thick NaCl films on Cu(111) (Fig. 1A). Previous studies (*14*, *15*) have shown that the adatoms can be switched reversibly between different charge states by applying suitable bias pulses with the STM tip. The NaCl layers are thin enough to permit the tunneling of electrons but can stabilize a single charge on the metal adatom through ionic relaxation in the NaCl film. The differently charged atoms have been identified by means of STM, scanning tunneling spectroscopy (STS), as well as comparison with density functional theory (DFT) (*14*, *15*). Below, we describe how we can resolve the charge state of individual atoms directly from AFM measurements.

In a constant-current STM measurement (Fig. 1B), a negatively charged gold adatom (Au^-) is identified by its surrounding depression (sombrero-shaped) and its smaller apparent height (h) [$h(Au^-) \approx$ 1.5 Å] with respect to a neutral Au adatom Au^0 [$h(Au^0) \approx 2.0$Å] (*14*). The same atoms were then imaged in constant-height mode, and the tunneling current (Fig. 1C) as well as the frequency-shift (Δf) signal (Fig. 1D) were recorded simultaneously. The larger absolute value of the tunneling current above Au^0 than above Au^- is in agreement with its larger apparent height in constant-current STM images. In the Δf image (Fig. 1D, inset), taken with NC-AFM, the adatoms are resolved as circular depressions with a diameter (full width at half maximum) of 6.5 and 5.5 Å for Au^0 and Au^-, respectively. The peak frequency shift measured above the negatively charged Au^- [$\Delta f(Au^-) = -1.86$ Hz] is, in absolute values, greater than above Au^0 [$\Delta f(Au^0) = -1.39$ Hz]. Figure 2A shows constant-height line scans above these two adatoms recorded at decreasing tip-to-sample distances Δz.

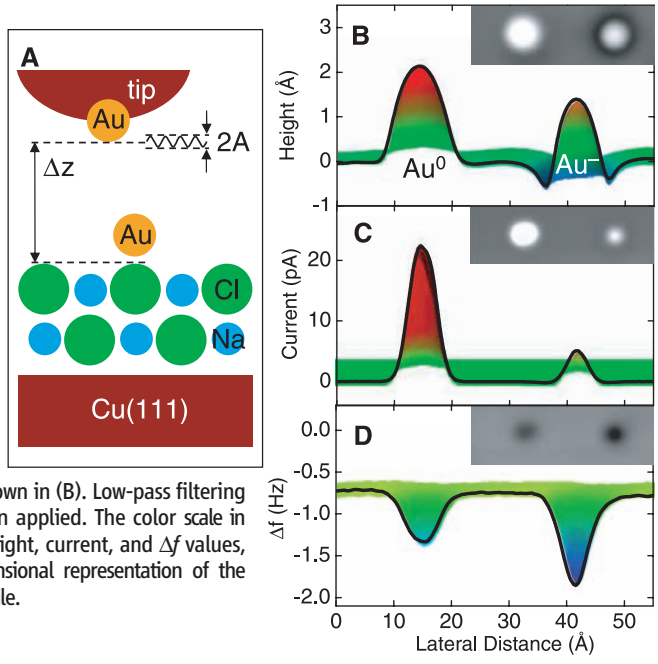

Fig. 1. (**A**) Model of the tip-sample geometry, showing the definition of the oscillation amplitude A and the tip height Δz (*26*). (**B**) Constant-current STM measurement [V = –50 mV and current (I) = 2 pA] of Au^0 (left) and Au^- (right) adsorbed on NaCl(2 ML)/Cu(111). The line scan is through the center of both atoms shown in the inset (image size of insets is 55 Å by 17 Å). (**C**) Current and (**D**) frequency shift recorded simultaneously in a constant-height measurement (Δz = 5.0 Å, V = –5 mV, and A = 0.3 Å) of the same area as shown in (B). Low-pass filtering (adjacent averaging) has been applied. The color scale in (B) to (D) corresponds to the height, current, and Δf values, respectively, in a three-dimensional representation of the images, cut along the line profile.

We used the method described by Sader and Jarvis (*28*) to deconvolve the oscillation amplitude from Δf and extract the vertical force from the constant-height line scans (*26*). In Fig. 2B, we plot the vertical force component; the background of the force from the substrate has been subtracted. The line scan at closest tip approach, corresponding to a tip height of 4.8 Å, shows an attractive force that is 11 pN greater above the negatively charged Au atom than it is above the neutral atom. The resolution in the force was better than 1 pN, and the charged atom could already be detected at a tip height of 6 Å, revealing a force that is about 2 pN greater than that above Au^0. A very high stability of the experimental system was needed for measuring forces in the piconewton regime. Charge screening by the insulating film [that is, ionic relaxations in the topmost NaCl layer as inferred from DFT calculations (*14*, *15*)] and image charges at the Cu interface make the forces so small. Approaching the tip further in order to increase the forces resulted in unintended charge switching and lateral manipulation of the adatoms.

It is known from DFT calculations that a Au adatom relaxes by about 0.4 Å toward the substrate when it becomes negatively charged (*14*). Just from this topographic difference, we would expect an effect in the direction opposite (a decrease of $|\Delta f|$) to that of the observed shift. We assigned the observed shift above the negatively charged Au^- to electrostatic interactions that overcompensate the topographic effect.

We investigated the switching event itself and its effect on the frequency shift and on the LCPD by measuring Δf with respect to the sample bias V. We specify the LCPD from measurements of V_{CPD} = (1/e) × LCPD (where e is the electron charge) by determining the peak position of the parabola obtained in a $\Delta f(V)$ measurement at a given tip position. The corresponding maximum in $\Delta f(V)$ is Δf^*, that is, Δf at compensated V_{CPD}. Without changing the tip height and position, we first (i) measured $\Delta f(V)$ above Au^-, then (ii) applied a bias voltage pulse of about –1 V so as to

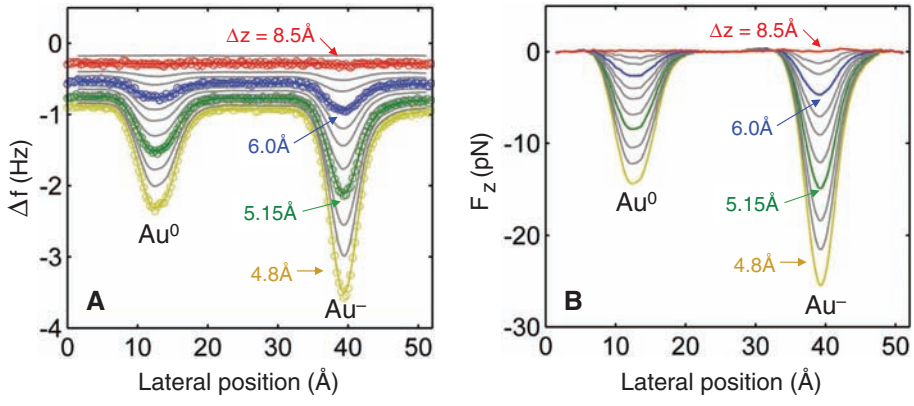

Fig. 2. (**A**) Frequency shift Δf recorded at a constant height (A = 0.22 Å and V = –2 mV) above Au^0 and Au^-. Different line scans correspond to different tip heights Δz as indicated. For some curves, every eighth point of the raw data are shown as an open circle in Fig. 2A; the solid lines correspond to the averaged data. (**B**) Vertical force F_z* extracted from the averaged data in (A) with the oscillation amplitude deconvolved and the constant background force subtracted from each curve (*26*).

switch the charge state (*14*), and finally (iii) measured $\Delta f(V)$ once more, as shown in Fig. 3A (*26*). To confirm that the switching event occurred and to verify that the switched atom did not change its lateral position, STM images were taken before and after this routine (Fig. 3, B and C). Performing the measurement under these conditions, and without moving the tip, ensured that the observed effects did not arise from tip changes, different tip heights, or spatial variations of the LCPD of the substrate. For typical experimental parameters, such as A = 0.6 Å and Δz = 5.8 Å, which result in a total frequency shift of about Δf = –3 Hz, we observed that the V_{CPD} of Au^- shifted by (+27 ± 8) mV with respect to Au^0. The corresponding Δf^* shifted by (–0.11 ± 0.03) Hz on Au^- as compared with Au^0.

Quantitatively, these values crucially depend on the exact tip shape (*9*, *29*), but we always observe a larger attractive force (a larger $|\Delta f^*|$) and a larger LCPD for Au^- than for Au^0. We attribute the shift in $|\Delta f^*|$ primarily to the interaction of the charged atom and its image charge induced in the AFM tip that was negligible in previous experiments (*19*, *23*, *26*). However, this is the main contribution to the observed contrast in Fig. 1D and Fig. 2. The shift in the LCPD can be explained by a dipole moment directed from the vacuum to the surface and induced by the negative Au^- (and its screening charge in the underlying substrate). Hence, the work function at the adatom position increases locally (*8*); the sample has to be biased more positively to compensate for the negative charge on the adatom.

To prove that positive, neutral, and negative charge states can be distinguished and determined with AFM, we included measurements of silver adatoms. For Ag, both the neutral Ag^0 and the positively charged Ag^+ adatoms are stable on NaCl(2 ML)/Cu(111) (*15*). Figure 4A shows a STM measurement of Au and Ag adatoms in their different possible charge states. Several $\Delta f(V)$ measurements were performed above these atoms at different tip-sample separations Δz, without a tip change between measurements and without switching the charge states. For each $\Delta f(V)$ measurement, we determined the peak position of the parabola, meaning the LCPD and the corresponding Δf^*. Figure 4B shows the LCPD plotted versus the tip height Δz. First, we compared the LCPD of NaCl(2 ML)/Cu(111) with that of the bare Cu(111) surface. The NaCl layer lowers the work function of the Cu surface, so we expected a decrease of the LCPD of NaCl(2 ML)/Cu(111) with respect to that of Cu(111). This is exactly what we observed, but in addition this effect increases with decreasing Δz. The latter observation is explained by an averaging effect, in which the sample area that contributes to the LCPD becomes larger with increasing Δz. The closer we approach the tip toward the NaCl island, the smaller the effect of the surrounding Cu(111) surface becomes, which explains the shift to smaller LCPD as the tip approaches the NaCl island (*26*).

For tip heights larger than 18 Å, the LCPD above the adatoms on the NaCl island are of similar value (within 100 mV). At smaller Δz, the effects arising from the adatom predominate, and the differently charged atoms can be distinguished by their LCPD for Δz < 10 Å. We observed that the LCPD of Ag^+ is smaller and that the LCPD of Au^- is larger than that of the corresponding neutral adatoms. The absolute values of these differences depend on the tip shape, but the direction of the LCPD shift is always determined by the direction of the dipole induced by the charged adatom.

In Fig. 4C, we plot the LCPD as a function of Δf^* for the same data as shown in Fig. 4B. This representation corresponds to a KPFM measurement and shows the LCPD at a given frequency shift with the contact potential compensated. Measuring these values at constant height without a feedback loop for either Δz or V (which is in contrast to usual KPFM measurements) increases the stability and sensitivity and allows the use of small oscillation amplitudes. In Fig. 4C, the contrast between the different species increases with more negative values of Δf^*. With decreasing Δz (and hence increasing $|\Delta f^*|$), the effect of the single atom becomes more pronounced as compared with the background forces from the substrate, and we observe that the LCPD shifts into different directions for the differently charged atoms. These measurements demonstrate that the charge state of neutral, positively, and negatively charged adatoms can be determined by measuring their LCPD at a certain tip height Δz or frequency shift Δf.

It should be possible to measure the transport of single-electron charges on insulating surfaces. For example, single atoms or small clusters acting as redox sites could be connected with molecules to form metal-molecular networks. By using the tip for charging the redox

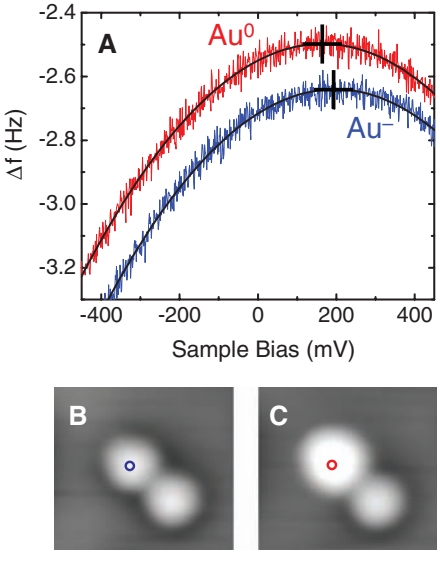

Fig. 3. (**A**) Frequency shift measured as a function of the voltage above Au^- and Au^0. Both measurements are performed without moving the tip (A = 0.6 Å and Δz = 5.8 Å; raw data). After measuring $\Delta f(V)$ above Au^-, the charge state is switched to Au^0 by applying a bias pulse of V = –1 V for a few seconds (*26*). Parabolic fits and corresponding parabola peaks are indicated. STM images (I = 7.4 pA, V = –50 mV, and size = 29 Å by 27 Å) before (**B**) and after (**C**) the $\Delta f(V)$ measurements confirm the charge-switching event and show that the switched Au atom has maintained its lateral position.

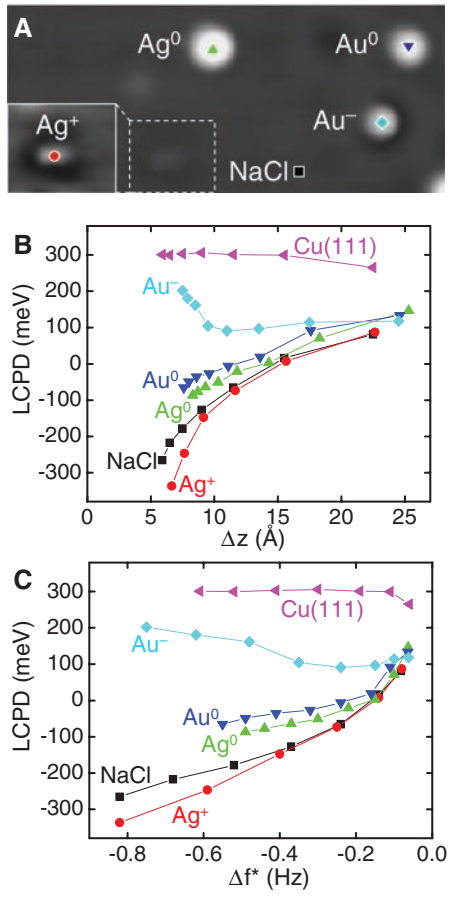

Fig. 4. (**A**) Constant-current STM image (I = 3 pA, V = 200 mV, and size = 130 Å by 60 Å) of Ag^+, Ag^0, Au^0, and Au^- on NaCl(2 ML)/Cu(111). The inset shows the Ag^+ adatom with fivefold increased z-contrast. (**B**) LCPD above atoms with different charge states and on NaCl(2 ML)/Cu(111) at the positions indicated in (A) and on Cu(111). At each site, $\Delta f(V)$ is measured for different tip heights Δz with respect to the NaCl surface [on Cu(111) with respect to point of contact with the metal]. Each $\Delta f(V)$ measurement is fitted with a parabola, yielding the LCPD and the corresponding frequency shift Δf^*. LCPD is shown as a function of Δz. (**C**) LCPD shown as a function of Δf^*; that is, corresponding to a KPFM measurement. The complete set of measurements has been performed without a tip change between measurements (*29*). Lines serve as a guide to the eye. The errors in Δz, LCPD, and Δf^* estimated from repeated measurements are ±0.2 Å, ±15 meV, and ±30 mHz, respectively.

sites, electrons can be injected into this network, and their propagation in the network could be observed with NC-AFM as described above. While STM is not ideally suited for this purpose because it relies on the tunneling of electrons (the unintended charging caused by the measurement and discharging of the structures via the substrate constitute a problem in STM experiments), we have shown that electrostatic AFM can enable the investigation of the charge landscape and of charge transport in metal-molecular nanostructures with atomic resolution.

References and Notes

1. Y. Sugimoto *et al.*, *Nature* **446**, 64 (2007).
2. Y. Sugimoto *et al.*, *Nat. Mater.* **4**, 156 (2005).
3. Y. Sugimoto *et al.*, *Science* **322**, 413 (2008).
4. M. Ternes, C. P. Lutz, C. F. Hirjibehedin, F. J. Giessibl, A. J. Heinrich, *Science* **319**, 1066 (2008).
5. M. Nonnenmacher, M. P. O'Boyle, H. K. Wickramasinghe, *Appl. Phys. Lett.* **58**, 2921 (1991).
6. S. Kitamura, K. Suzuki, M. Iwatsuki, C. B. Mooney, *Appl. Surf. Sci.* **157**, 222 (2000).
7. K. Okamoto, Y. Sugawara, S. Morita, *Appl. Surf. Sci.* **188**, 381 (2002).
8. M. Ikeda, N. Koide, L. Han, A. Sasahara, H. Onishi, *J. Phys. Chem. C* **112**, 6961 (2008).
9. G. H. Enevoldsen, T. Glatzel, M. C. Christensen, J. V. Lauritsen, F. Besenbacher, *Phys. Rev. Lett.* **100**, 236104 (2008).
10. F. Bocquet, L. Nony, C. Loppacher, T. Glatzel, *Phys. Rev. B* **78**, 035410 (2008).
11. K. Uchida, in *Nanoelectronics and Information Technology: Advanced Electronic Materials and Novel Devices*, R. Waser, Ed. (Wiley, New York, 2003), chap. 16.
12. K. K. Likharev, *IEEE Proc.* **87**, 606 (1999).
13. M. Haruta, *Catal. Today* **36**, 153 (1997).
14. J. Repp, G. Meyer, F. E. Olsson, M. Persson, *Science* **305**, 493 (2004).
15. F. E. Olsson, S. Paavilainen, M. Persson, J. Repp, G. Meyer, *Phys. Rev. Lett.* **98**, 176803 (2007).
16. M. Sterrer *et al.*, *Phys. Rev. Lett.* **98**, 096107 (2007).
17. C. Schoenenberger, S. F. Alvarado, *Phys. Rev. Lett.* **65**, 3162 (1990).
18. L. J. Klein, C. C. Williams, *Appl. Phys. Lett.* **79**, 1828 (2001).
19. R. Stomp *et al.*, *Phys. Rev. Lett.* **94**, 056802 (2005).
20. J. Zhu, M. Brink, P. L. McEuen, *Appl. Phys. Lett.* **87**, 242102 (2005).
21. E. Bussmann, N. Zheng, C. C. Williams, *Appl. Phys. Lett.* **86**, 163109 (2005).
22. E. Bussmann, C. C. Williams, *Appl. Phys. Lett.* **88**, 263108 (2006).
23. Y. Azuma, M. Kanehara, T. Teranishi, Y. Majima, *Phys. Rev. Lett.* **96**, 016108 (2006).
24. F. J. Giessibl, *Rev. Mod. Phys.* **75**, 949 (2003).
25. F. J. Giessibl, *Appl. Phys. Lett.* **76**, 1470 (2000).
26. Materials and methods are available as supporting material on *Science* Online.
27. T. Albrecht, P. Grütter, D. Horne, D. Rugar, *J. Appl. Phys.* **69**, 668 (1991).
28. J. E. Sader, S. P. Jarvis, *Appl. Phys. Lett.* **84**, 1801 (2004).
29. We observed that the LCPD and Δf^* are crucially dependent on the tip. However, the direction of the observed shifts in the LCPD and in Δf^* because of the atoms' charge state are not tip-dependent, allowing the determination of the charge states by comparison. In general, we observed higher shifts in the LCPD for smaller tip-sample separations and for tips exhibiting a small background force (that is, presumably very sharp tips).

30. We thank R. Allenspach for valuable comments. This work was supported by the Swiss National Center of Competence in Research (NCCR) "Nanoscale Science" and by the European Union project "NanoMan." P.L. and J.R. gratefully acknowledge funding by the Nederlandse Organisatie voor Wetenschappelijk Onderzoek (Chemical Sciences, Vidi-grant 700.56.423) and Volkswagen Foundation through its Lichtenberg program, respectively.

Supporting Online Material

www.sciencemag.org/cgi/content/full/324/5933/1428/DC1
Materials and Methods
SOM Text
Figs. S1 and S2
References

13 February 2009; accepted 1 May 2009
10.1126/science.1172273

Oxygen-18 of O_2 Records the Impact of Abrupt Climate Change on the Terrestrial Biosphere

Jeffrey P. Severinghaus,[1]* Ross Beaudette,[1] Melissa A. Headly,[1]† Kendrick Taylor,[2] Edward J. Brook[3]

Photosynthesis and respiration occur widely on Earth's surface, and the $^{18}O/^{16}O$ ratio of the oxygen produced and consumed varies with climatic conditions. As a consequence, the history of climate is reflected in the deviation of the $^{18}O/^{16}O$ of air ($\delta^{18}O_{atm}$) from seawater $\delta^{18}O$ (known as the Dole effect). We report variations in $\delta^{18}O_{atm}$ over the past 60,000 years related to Heinrich and Dansgaard-Oeschger events, two modes of abrupt climate change observed during the last ice age. Correlations with cave records support the hypothesis that the Dole effect is primarily governed by the strength of the Asian and North African monsoons and confirm that widespread changes in low-latitude terrestrial rainfall accompanied abrupt climate change. The rapid $\delta^{18}O_{atm}$ changes can also be used to synchronize ice records by providing global time markers.

The mechanism of abrupt climate change, in particular the Heinrich and Dansgaard-Oeschger (D/O) events of the last ice age, remains poorly understood (*1*). One barrier is the dearth of information about the spatial extent of the events, due in part to the paucity of low-latitude paleoclimate records with sufficient dating precision to establish whether events are synchronous, time-transgressive, or unrelated (*2*). Cave stalagmite $\delta^{18}O$ records with radiometric U/Th dating are a notable exception (*3*–*6*), but these are still spot records with generally unknown spatial importance. Atmospheric gas records from ice cores can help address the spatial issue because the atmosphere acts as an integrator of innumerable gas fluxes over broad spatial scales. Methane has been used in this capacity (*7*), but methane production is dominated by rather special settings (e.g., high-productivity anoxic wetland soils). Oxygen (O_2), in contrast, is produced widely in the low latitudes by photosynthesis, making it a more ideal tracer of the spatial extent and global importance of climate change. In particular, the isotopic composition of oxygen produced on land varies strongly with environmental conditions, making it a unique tracer of the impact of climate on the terrestrial biosphere (*8*–*11*).

The $^{18}O/^{16}O$ ratio of atmospheric molecular oxygen ($\delta^{18}O_{atm}$) is known to vary on orbital time scales in response to the growth of ice sheets and changes in biogeochemical fractionation (*8*–*11*), with a typical glacial-interglacial range of ~1.5 per mil (‰). The substrate for all photosynthetic oxygen production is water, and the isotopic composition of the water ($H_2{}^{18}O/H_2{}^{16}O$) in which photosynthesis occurs is transferred to O_2 (*12*). Thus, variations in water $\delta^{18}O$ at the site of photosynthesis (i.e., the chloroplast) are a primary cause of variation in $\delta^{18}O_{atm}$ (*13*). Ice sheet growth and decay, with attendant change in seawater $\delta^{18}O$ (and thus all meteoric water), causes roughly half of the variation. The balance is due to changes in hydrological cycle fractionation during condensation and evaporation that affect chloroplast water $\delta^{18}O$, and fractionation by the respiratory sink of O_2 (*10*, *11*). These fractionation processes collectively create a steady-state offset between seawater $\delta^{18}O$ and the $\delta^{18}O$ of O_2, known as the Dole effect, which today amounts to +23.88‰ (*14*).

Past variations in the Dole effect are known to occur on orbital time scales, chiefly the 23,000-year (23 ky) precession period (*10*, *11*). These variations are likely due to the Asian and African monsoon variations that occur on this time scale because of the impact of precession on summer insolation (*15*, *16*), although other factors may also contribute, and the subject is currently not well understood. Faster variations have generally not been expected because of the ~1000-year turnover time of atmospheric O_2.

[1]Scripps Institution of Oceanography, University of California, San Diego, CA 92093–0244, USA. [2]Desert Research Institute, Nevada System of Higher Education, 2215 Raggio Boulevard, Reno, NV 89512, USA. [3]Department of Geosciences, Oregon State University, Corvallis, OR 97331, USA.

*To whom correspondence should be addressed. E-mail: jseveringhaus@ucsd.edu

†Present address: The Pennington School, 112 West Delaware Avenue, Pennington, NJ 08534, USA.